Progress In Electromagnetics Research C, Vol. 137, 251–262, 2023

Coupling Analysis of Multi-Physical Fields of Magnetic Gear Motor with Nonuniform Air-gap Halbach Array Magnetization

Zhangtao Kui, Kun Yang, Weizhao Tang, and Libing Jing*

Abstract—In this paper, a novel magnetic gear motor (MGM) with nonuniform air gap Halbach array magnetization is proposed to study the influence of temperature change on its electromagnetic performance. The inner PM adopts the Halbach array magnetization structure, which makes the inner rotor air gap have an uneven air gap structure, thereby improving the air gap flux density. In addition, the air gap magnetic field of MGM is analyzed by the finite element method (FEM), and the 3D model of the motor is established. The main losses of the motor, including copper loss, eddy current loss, and hysteresis loss are coupled to each component as a thermal source and studied by magneto-thermal coupling. The transient variation characteristics of loss distribution during MGM operation are comprehensively considered. The temperature variation of each component of the MGM with time during load operation is studied in detail. The results show that the temperature of the PM of the MGM is close to 91.8°C when the rated load is running, and the PM of the motor does not undergo irreversible demagnetization.

1. INTRODUCTION

The magnetic gear motor (MGM) has the advantages of high torque density, small torque ripple, high efficiency, and strong reliability. Therefore, it is widely used in wind power generation, electric vehicles, ship propulsion, and other low-speed and high-torque fields [1, 2]. However, during the operation of the motor, the temperature rise has a great impact on its performance, especially the overheating of the permanent magnet (PM) leads to irreversible demagnetization, thus affecting the reliability of the motor [3]. Based on this consideration, it is of great significance to analyze the temperature field in the design and analysis of MGM.

The research on the temperature field of the motor uses the equivalent thermal network method and finite element method (FEM) which can accurately simulate and calculate the temperature field of the motor [4]. In [5], the thermal analysis of a new linear motor was carried out by using the three-dimensional (3D) piecewise equivalent thermal circuit model. In [6], the concept of lumped parameters was used to convert the temperature field of the motor into an equivalent thermal network. The equivalent thermal network method has the advantages of fast calculation speed and high accuracy. However, in order to understand the temperature distribution of the motor more comprehensively, it is necessary to increase the number of network nodes in the temperature field, resulting in increased calculation and reduced efficiency [7].

The application of the FEM in motor temperature analysis can realize the flexible division of each part of the motor and make the calculation more accurate [8]. At the same time, combined with the coupling method of the electromagnetic field and temperature field, the transient variation characteristics of motor loss and temperature distribution at any time can be studied, and their variation

---

Received 14 June 2023, Accepted 2 September 2023, Scheduled 15 September 2023

* Corresponding author: Libing Jing (jinglibing163@163.com).
The authors are with College of Electrical Engineering & New Energy, Hubei Provincial Engineering Technology Research Center for Microgrid, China Three Gorges University, Yichang 443002, China.

rules can be deeply explored [9]. In [10], the electromagnetic field-thermal-stress field coupling model was used to analyze the main performance of the motor through FEM. Based on lumped parameter thermal network, the electromagnetic field and thermal field are coupled [11]. This method can accurately evaluate the electromagnetic performance and thermal performance at the design stage. The 3D uniform distribution of magnet loss is considered [12], and the electromagnetic loss of the motor is calculated by the 3D transient FEM. By loading the actual loss distribution into the three-dimensional thermal model, the accuracy of the motor loss and temperature rise calculation results is improved. Although there are a lot of studies on the multi-physical field characteristics and temperature distribution of PM motors, there are few studies on the multi-physical field analysis of MGM.

In this paper, the field-circuit coupling method is used to solve and analyze the magnetic field and temperature field of MGM. In this method, the loss of each part of the motor is coupled to the temperature field as a thermal source, and the temperature field analysis results are fed back to the electromagnetic field analysis, thus avoiding the error caused by the artificial introduction of the thermal source, and the spatial distribution characteristics of the temperature rise of the main components of the motor are calculated by multiple iterations. In Section 2, the topology of the motor is introduced, and its magnetic field is analyzed. In Section 3, the thermal conductivity and thermal dissipation coefficient of each component of the motor is analyzed. In Section 4, the field-circuit coupling method is used to study the temperature field of the MGM. Finally, some conclusions are drawn in Section 5.

2. MAGNETIC FIELD ANALYSIS

In this paper, a nonuniform air gap Halbach array MGM is studied by the research group. Its structure has an inner and outer air gap, which includes a stator, a magnetic tooth, an outer rotor, and an inner rotor. The PM of the outer rotor adopts a spoke array structure. The PM of the inner rotor adopts a nonuniform air gap and adopts a Halbach array magnetization structure. The stator armature winding adopts a double-layer winding with 9 slots and 8 poles. Fig. 1 shows the 2D topology of the proposed MGM. The main parameters of the motor are listed in Table 1.

Table 1. Parameters of the proposed model.

Parameter	Value
Outer radius of stator (mm)	102
Stator yoke radius (mm)	93.1
Stator tooth radius (mm)	91.7
Outer radius of modulation tooth (mm)	85.4
Inner radius of modulation tooth (mm)	80.6
Axial length (mm)	100
Outer/Inner rotor speed (rpm)	130/750
Number of stator slots	9
Winding turns	3
Winding pitch	1
Pole-pairs number of outer/inner rotor PM	23/4
PMs material	NdFeB
PM mass (kg)	4.50
Motor volume (m^3)	3.4×10^{-3}

According to the no-load magnetic field distribution of MGM shown in Fig. 2, it can be seen that the magnetic field line passes through the inner and outer air gaps, starting from the N pole of the inner PM in turn, passing through an inner air gap, outer rotor, outer air gap, magnetic tooth, stator core, magnetic tooth, outer air gap, outer rotor, inner air gap, and finally reaches the inner rotor PM S pole,

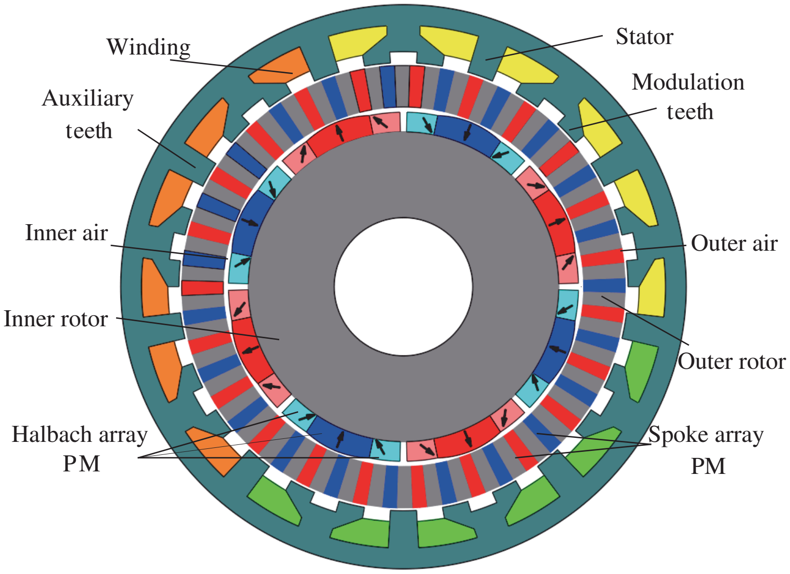

Figure 1. 2D topology of the motor.

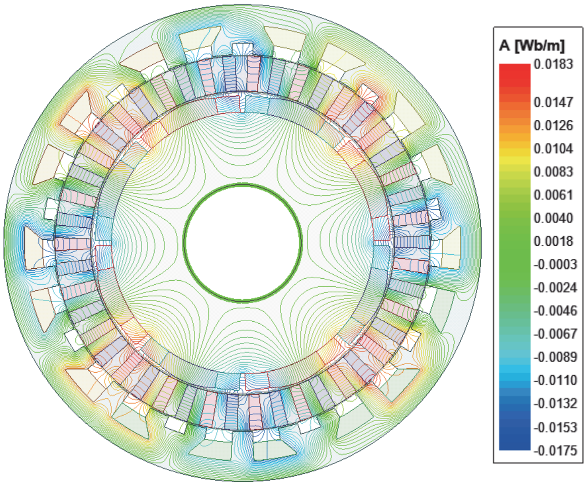

Figure 2. Distribution of no-load magnetic field lines.

forming a series magnetic circuit. The magnetic field generated by the inner rotor PM interacts with the harmonics generated by the outer rotor PM through magnetic tooth modulation. The spoke array PMs have a magnetic concentration effect, which increases the magnetic flux density of the inner and outer air gaps and reduces the magnetic flux leakage. The Halbach array PMs have a unilateral magnetic concentration effect, which improves the magnetic flux distribution of the inner rotor and increases the magnetic flux density of the inner air gap, which is beneficial for improving the output torque of the MGM. The magnetomotive force generated by the rotor PM interacts with the alternating permeance, which produces a series of harmonics in the air gap. Therefore, the air gap harmonic pole pairs also satisfy the following equation,

$$P_{nm} = \quad |nP_r \pm mZ| \quad n = 1, 3, 5 \ldots \quad m = 0, 1, 2, 3 \ldots \tag{1}$$

where P_{nm} is the harmonic pole pair; n and m are the harmonic order; P_r is the inner rotor PM pole pairs; and Z is the modulation teeth. When $n = 1$, the 4th, 23rd, 31st, 50th, and 58th harmonic components are working harmonics. These working harmonics have the same number of magnetic poles, the same speed and direction, and can promote energy transfer in the air gap.

According to the outer air gap radial flux density waveform and harmonic spectrum shown in Fig. 3, it can be found that there are a large number of harmonic components in the outer air gap flux density waveform curve of the motor. By further analyzing the harmonic spectrum, it is found that the outer rotor Spoke structure has a magnetic focusing effect, and the amplitude of 4, 23, 31, and 50 working harmonics increases, which helps the torque to be transmitted in the outer air gap. In addition, the amplitude of 42 non-working harmonics increases, which improves the loss of the motor.

Figure 4 shows the waveform and harmonic spectrum of the radial magnetic density in the inner air gap. The results show that the magnetic density waveform curve of the inner air gap is an approximate sine curve. By using the Halbach array, the sinusoidal distribution of the magnetic field in the air gap is higher, and the influence of the harmonic magnetic field is smaller. From the harmonic spectrum analysis, it can be concluded that the amplitude of the 4th and 23rd working harmonics is high, and the non-working harmonics are effectively suppressed.

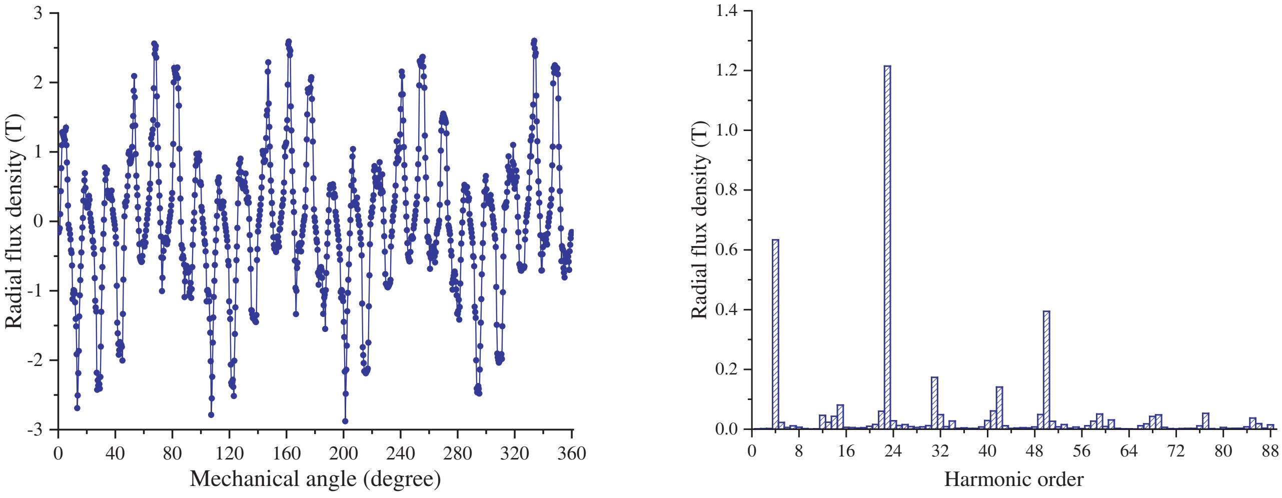

(a) (b)

Figure 3. Radial flux density in the outer air gap. (a) Waveform. (b) Harmonic spectra.

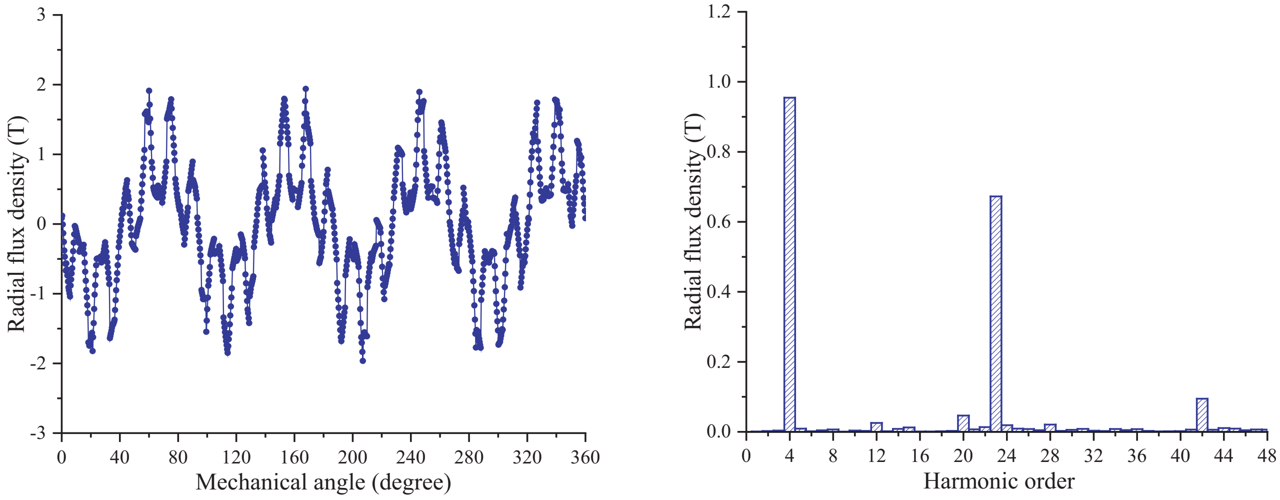

(a) (b)

Figure 4. Radial flux density in the inner air gap. (a) Waveform. (b) Harmonic spectra.

3. DETERMINATION OF SOLUTION CONDITIONS

3.1. Analysis of Thermal Field Mathematical Model

The magnetic thermal coupling analysis of the MGM is carried out by the FEM, and the temperature field analysis is carried out by solving the numerical solution of the differential equation of the discrete mathematical model of the motor. In addition, the initial temperature and boundary conditions of the environment need to be set before solving. The initial temperature of the environment refers to the instantaneous temperature distribution when $t = 0$, and the boundary condition refers to the thermal exchange between the surface and the surrounding medium. The common boundary conditions are as follows [13]

$$\begin{cases} -k_q \dfrac{\partial T}{\partial n}\bigg|_{S_2} = q_0 \\ T_{s_1} = T_0 \\ -k_q \dfrac{\partial T}{\partial n}\bigg|_{S_3} = \alpha_q \left(T - T_f\right) \end{cases} \tag{2}$$

where q_0 is the thermal flux of the boundary surface of the first boundary condition, and T_0 is the initial temperature value of the second boundary condition. The thermal transfer coefficient and temperature on both sides of the boundary are the third boundary conditions. S_1, S_2, and S_3 are boundary surfaces; k_q is the boundary thermal conductivity; α_q is the thermal transfer coefficient; and T_f is the temperature around the thermal dissipation surface.

3.2. Calculation of Thermal Conductivity and Thermal Dissipation Coefficient

The loss generated by the motor during operation is converted into heat, which increases the temperature of each part of the motor. The thermal transfer process is a comprehensive process of thermal conduction and thermal convection. The above process is closely related to the thermal conductivity coefficient and thermal loss coefficient of each material of MGM.

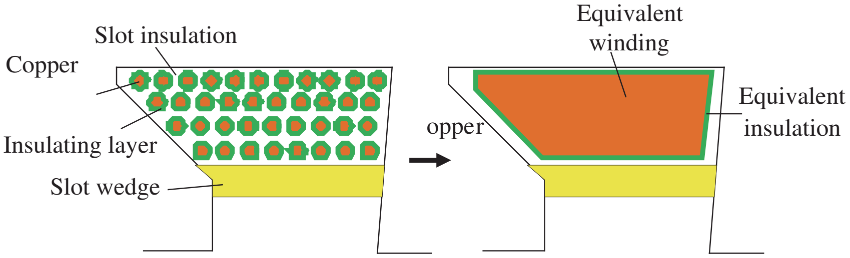

Figure 5. Equivalent winding.

When establishing the magneto-thermal coupling model, the stator winding model is simplified as follows; the copper wire of the winding is equivalent to a conductor with equal volume; and the insulating material such as the insulating layer of the wire and the insulating paint between the wires is equivalent to a thermal conduction layer evenly distributed around the equivalent winding. Fig. 5 shows the equivalent winding. The equivalent thermal conductivity of the stator winding is as follows [14].

$$\alpha_r = \frac{\delta_k + \delta_0 + \delta_x}{\delta_k/\alpha_k + \delta_0/\alpha_0 + \delta_x/\alpha_x} \tag{3}$$

where δ_k and α_k are the thickness and thermal conductivity of the wire insulation in the thermal flow direction; δ_0 and α_0 are the thickness and thermal conductivity of air and insulating paint between wires, respectively. δ_x and α_x are the thickness and thermal conductivity of the conductor insulation layer, respectively.

The thermal transfer of each part of the motor is related to its material properties. At 25°C, the relevant parameters of each material are shown in Table 2.

Table 2. 25°C temperature field related parameters.

Unit	Material	Coefficient of thermal conductivity (W/(m · °C))	Density (Kg/m^3)	Specific thermal capacity (J/(Kg · °C))
Winding	Copper	387.6	8978	381
Stator and rotor core	Silicon steel	40	7800	460
Casing	Aluminum alloy	161	2750	890
PM	NdFeB	10	7550	440
Air gap	Air	0.0267	1.29	1000

The heat generated by the motor during operation needs to be dissipated from the inside through the surface. In order to determine the convective thermal dissipation coefficients of the casing surface, the stator end surface, the outer surface of the winding end, the outer rotor end surface, and the inner rotor end surface, the expressions of the convective thermal dissipation coefficients of the casing surface, the stator end surface, and the outer surface of the winding end are as follows,

$$\alpha_i = \frac{1 + 0.25v}{0.045} \tag{4}$$

where v is the flow rate of the gas medium during forced air cooling, and the unit is m^3/s. The convective thermal transfer coefficients of the rotor end faces are as follows,

$$\alpha_{ii} = 28(1 + \sqrt{0.45v}) \tag{5}$$

The heat is transferred to the outside through the air gap of the motor. To reduce the workload of simulation calculation, the equivalent convection thermal dissipation coefficient of air gap is introduced. The Reynolds number R_e in fluid mechanics is expressed as follows

$$R_e = \frac{4\pi R_r V l}{60A} \tag{6}$$

where R_r is the outer radius of the motor rotor, V the rotor speed, l the air gap thickness, and A the air viscosity coefficient. The expression of critical Reynolds number R_{ec} is as follows,

$$R_{ec} = 58.27\sqrt{\frac{R_2}{l}} \tag{7}$$

where R_2 is the inner radius of the stator. According to formulas (6) and (7), $R_e > R_{ec}$ can be obtained. It can be judged that the medium flow in the air gap is turbulent, and the equivalent thermal conductivity of the air gap is as follows,

$$\alpha = 0.0019\left(\frac{D_o}{R_2}\right)^{-2.9084} R_e^{0.4614\ln\left(3.33361\frac{D_o}{R_2}\right)} \tag{8}$$

where D_o is the outer diameter of the stator. According to the relevant formulas of thermal transfer, the convective thermal dissipation coefficient of each part of the MGM can be calculated. In this paper, the main parameters of the convective thermal dissipation coefficient of the MGM are calculated by combining theoretical analysis and empirical data [15], as shown in Table 3.

4. TEMPERATURE FIELD STUDY

During the operation of the motor, a certain amount of heat is generated. This heat causes the motor temperature to rise. If it exceeds the maximum temperature limit of the MGM, it affects the normal

Table 3. Convective thermal transfer coefficient of each component at 25°C.

Unit	Casing surface	Stator surface	Winding surface	Outer rotor surface	Inner rotor surface	Air gap
Thermal convection coefficient ($\mathrm{W/(m^2 \cdot {}^\circ C)}$)	22	22	22	54.46	61.52	0.2137

operation and life of the MGM. Therefore, it is necessary to analyze the thermal source of the motor to understand the generation and transmission path of the heat. The thermal source of the motor generally includes iron loss, copper loss, and stray loss. Among them, the iron loss is mainly caused by the alternating magnetic field, including eddy current loss, and hysteresis loss [16]. In this paper, the hysteresis loss, eddy current loss, and copper loss of the MGM are mainly analyzed. The calculation expression of the loss caused by the harmonic magnetic field in core is as follows,

$$P_{Fe} = P_e + P_h + P_a = k_e f_p B^{\alpha} + k_h f_p^2 B^2 + k_a f_p^{1.5} B^{1.5} \tag{9}$$

where P_{Fe}, P_e, P_h, and P_a are the iron loss, core eddy current loss, hysteresis loss, and additional loss of the motor, respectively; f_p is the frequency of the alternating magnetic field; B is the magnetic density amplitude; k_e, k_h, and k_a are the related loss coefficients of the material. Due to the alternating magnetic field, the permanent magnet produces eddy current loss. The simplified calculation formula of PM eddy current loss is as follows,

$$P_e = \frac{Vb^2h^2}{2\rho\left(b^2+h^2\right)} \sum_{n=1} n^2 f_n^2 B_n^2 \tag{10}$$

where V is the volume of the PM, b the average width of the PM, h the axial length of the PM, ρ the resistivity of the PM, n the harmonic number, f_n the relative motion frequency, and B_n the amplitude of the harmonic magnetic flux density.

At a rated current of 5A, Fig. 6 shows the core loss cloud diagram. It can be seen that the motor core loss is mainly concentrated in the stator and outer rotor parts. When the motor rotates at high speed, the current change frequency is high, and the reverse rotating armature reaction harmonic magnetomotive force component is strong, which induce large loss in the stator and rotor. In addition, the non-working harmonic amplitude also affects the loss.

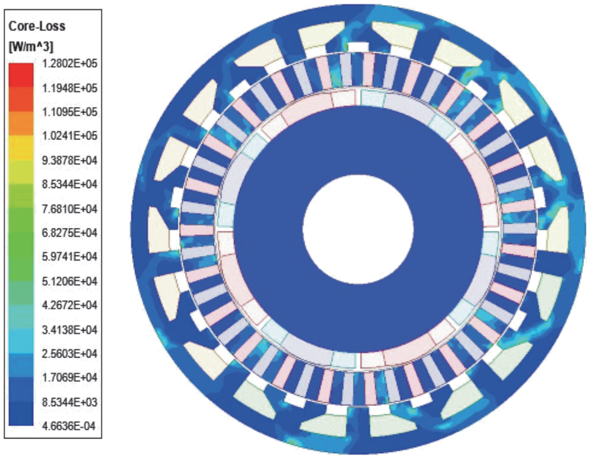

Figure 6. Core loss distribution cloud diagram.

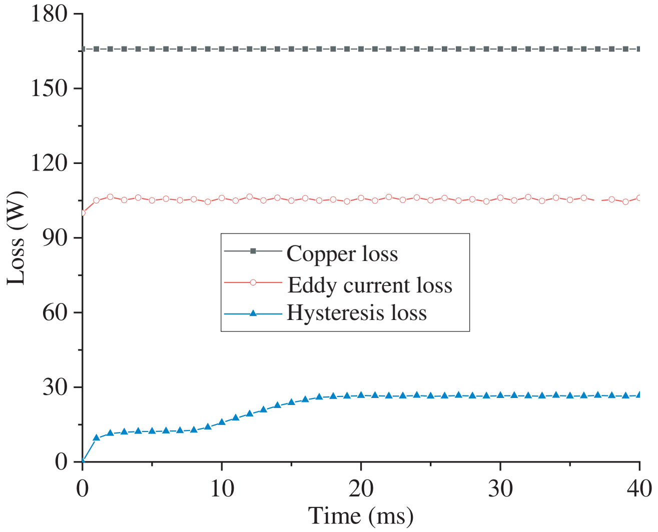

Figure 7. The loss changes of MGM.

The loss analysis of MGM is carried out in Maxwell. Fig. 7 is the distribution of the loss results of the MGM under the condition of ignoring the stray loss, that is, the internally generated heat. The winding copper loss of the motor accounts for a high proportion of 165.8 w, and eddy current loss and hysteresis loss are 106.3 w and 24 w, respectively. By analyzing the thermal source of the MGM and coupling the electromagnetic field analysis results with the temperature field analysis, the thermal transfer path of the motor can be obtained.

Figure 8(a) shows the thermal transfer path of the MGM thermal source. From the diagram, it can be seen that the thermal transfer of the MGM is as follows. The heat generated by the inner rotor contacts the inner air gap and transfers heat to the rotor and outer air gap. The heat generated by the outer rotor is transferred to the inner and outer air gaps. The heat generated by the armature winding is transmitted to the casing and air gap.

Through the establishment of the above motor thermal source and magneto-thermal coupling model, the temperature field 3D MGM model is established in the Solidworks and FEM software.

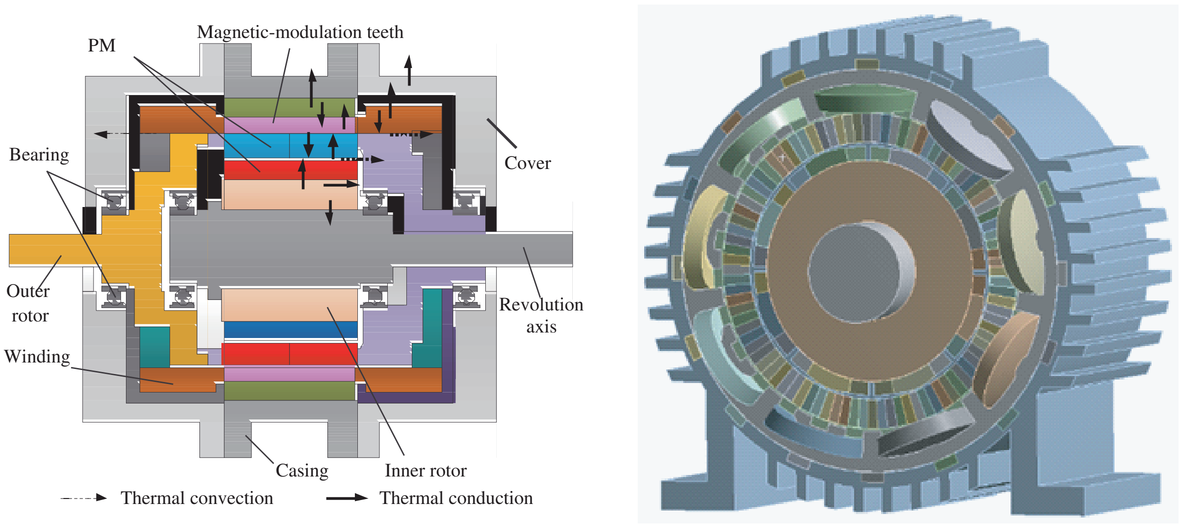

(a) (b)

Figure 8. (a) Thermal transfer path of thermal source. (b) Temperature field 3D motor model.

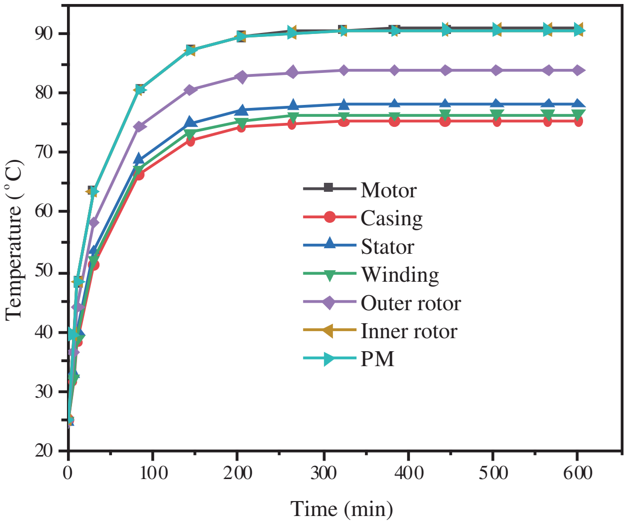

Figure 9. Temperature changes of each part of the MGM.

Maxwell and Workbench are used for joint simulation, as shown in Fig. 8(b), and the loss of the 2D model under rated conditions is coupled to the 3D temperature field as the thermal source of the motor [17]. The internal heat generation is sequentially coupled to Workbench and converted into thermal flux. Then it is applied to the MGM temperature field model for temperature field analysis. Finally, the temperature field distribution and temperature rise of MGM and its components are obtained. In the solution process, the simulation time is set to 600 min, the initial temperature of the environment set to 25°C, and the electromagnetic field and temperature field of the MGM are solved by 3D coupling at the rated working point for 10 hours. Fig. 9 shows the temperature change of MGM components with time under rated operating conditions. It can be concluded as follows,

1. In the early stage of operation, the components of the motor began to consume energy and produce a lot of heat, resulting in the rapid growth of the comprehensive temperature of the MGM before 100 min, and the overall temperature rose rapidly to 80°C. After 100 min, the temperature rise slowed down. After 200 min, the temperature change was small, and then basically stabilized at about 91°C. The temperature rise trend of the MGM components is close.
2. During the whole process, the armature winding temperature is high, because the winding produces a large amount of copper loss when the motor is running, and it is converted into thermal source. The temperature finally approaches 75°C. The shell is made of aluminum alloy with good thermal conductivity. The outer surface directly contacts the ambient air, and the thermal dissipation area is large, so the temperature is the lowest.
3. The rotor is affected by the air gap non-working harmonics, and the harmonic loss and core loss are large. As a result, the outer rotor temperature is high. In addition, the thermal dissipation of the inner rotor is difficult; the heat is difficult to transmit outward; and the final temperature tends to be 91°C.

The temperature field analysis results of the MGM and the temperature distribution of each component are shown in Fig. 10. Through the temperature field analysis, the temperature distribution of MGM components can be comprehensively evaluated. According to the temperature field analysis results of the MGM, the temperature distribution of each component is uneven, but the temperature of MGM components is within a reasonable range. Specifically, the temperature of the inner rotor and PM is relatively high, while the temperature of the motor shell and stator is relatively low. The reason for this uneven temperature distribution is mainly the different material properties, thermal generation, and thermal dissipation capacity of each component.

If the motor runs for a long time at a high temperature, it may cause the PM to demagnetize and cause failure. In addition, due to a series of problems such as temperature rise and torque reduction caused by PM demagnetization, the degree of PM demagnetization is further deepened, resulting in irreversible accidents such as motor shutdown and burning. Therefore, it is necessary to study and analyze the PM demagnetization of the motor [18, 19]. Fig. 11 shows the demagnetization analysis of

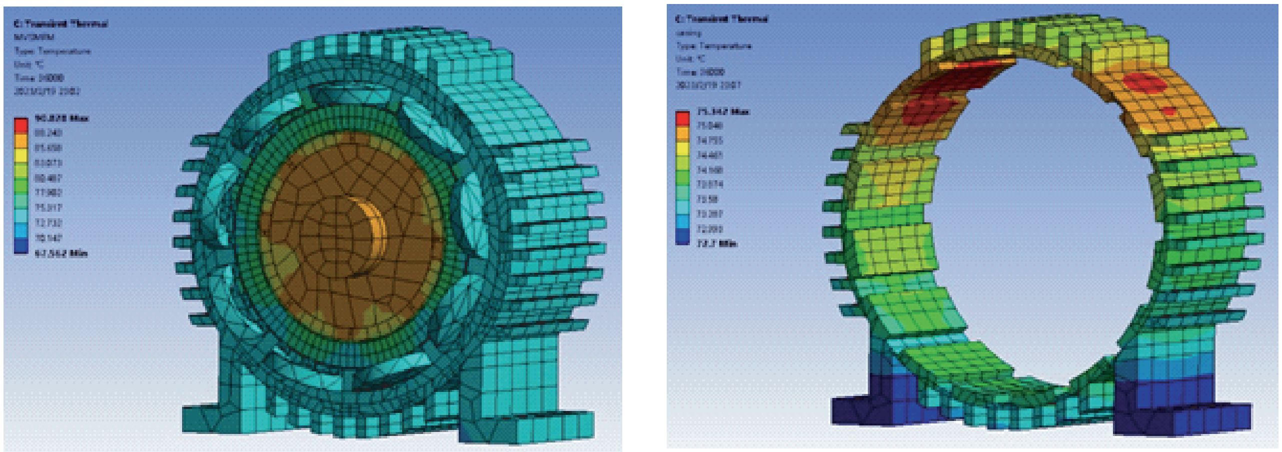

(a) The entire motor (b) Casing

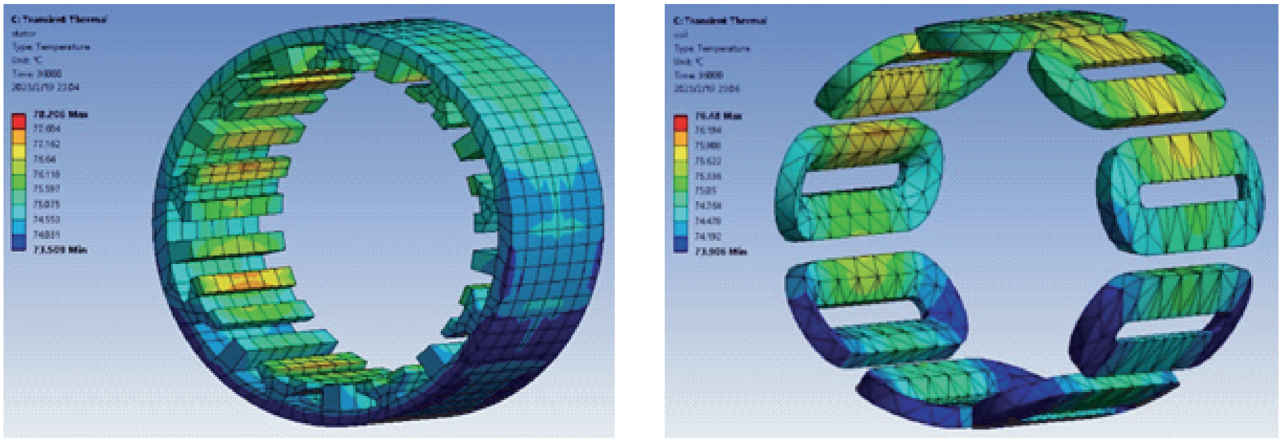

(c) Stator (d) Armature winding

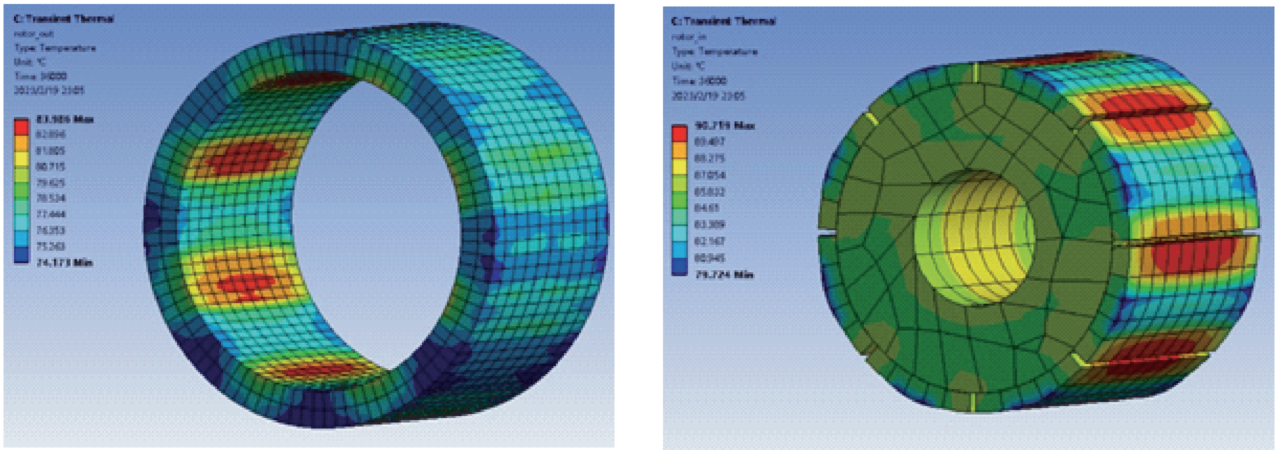

(e) Outer rotor (f) Inner rotor

Figure 10. Temperature field analysis results of MGM.

PM. Fig. 11(a) shows the temperature field analysis results of the inner and outer PMs. According to Fig. 9, PM temperature tends to be stable after 300 min, and the temperature distribution of PMs is not uniform, but the maximum temperature of PM does not exceed 100°C. Fig. 11(b) shows the demagnetization characteristics of NdFeB. There is no demagnetization inflection point on the curve at 100°C, so the PM of the MGM under rated conditions does not undergo irreversible demagnetization which shows that the performance of the proposed motor is good.

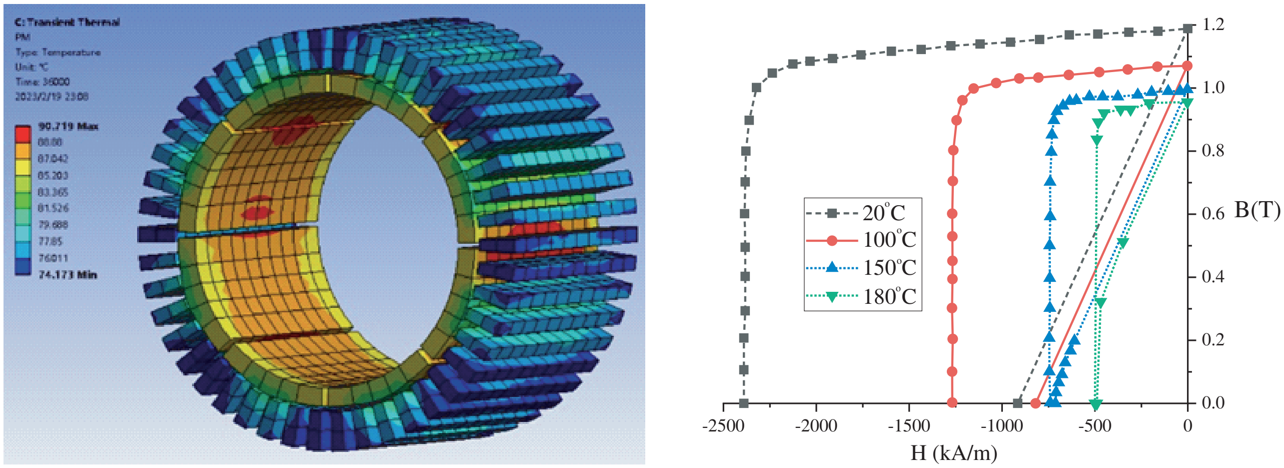

(a) (b)

Figure 11. Demagnetization analysis of PM. (a) Temperature field analysis results of PM. (b) Demagnetization characteristic curve of NdFeB.

5. CONCLUSION

In this study, a novel MGM with nonuniform air gap Halbach array magnetization is proposed. The magnetic-thermal coupling method is used to sequentially couple the power loss as a thermal source to each component of the MGM for 3D temperature field research. The multi-physical domain coupling of electromagnetic temperature field is realized, and the temperature research of the MGM is more accurate.

(1) When the MGM continues to operate at the rated operating point, the temperature of each component rises rapidly in the early stage, but with the passage of time, the temperature change gradually slows down. During the whole process, the temperature of PM and inner rotor as heating components is the highest, and the temperature of casing is the lowest. The temperature distribution of MGM components is not uniform, but the temperature is within a reasonable range, which is lower than 100°C.

(2) For the proposed magnetic field motor, the inner and outer PMs adopt Halbach array and Spoke array, respectively, which makes the motor have better air gap flux density and smaller magnetic flux leakage and reduces the non-working harmonic amplitude in the air gap. By analyzing the PM temperature field, the PM under rated conditions does not undergo irreversible demagnetization.

REFERENCES

1. Jo, I.-H., H.-W. Lee, G. Jeong, W.-Y. Ji, and C.-B. Park, "A study on the reduction of cogging torque for the skew of a magnetic geared synchronous motor," *IEEE Trans. Magn.*, Vol. 55, No. 2, 1–5, Feb. 2019.
2. Aiso, K., K. Akatsu, and Y. Aoyama, "A novel reluctance magnetic gear for high-speed motor," *IEEE Trans. Ind. Appl.*, Vol. 55, No. 3, 2690–2699, May–Jun. 2019.

3. Tang, H., J. Di, Z. Wu, and W. Li, "Temperature analysis for the asymmetric six-phase permanent magnet synchronous motor in healthy and fault-tolerant modes," *IEEE Trans. Ind. Electron.*, Vol. 70, No. 7, 6482–6493, Jul. 2023.
4. Huang, X., Q. Tan, L. Li, J. Li, and Z. Qian, "Winding temperature field model considering void ratio and temperature rise of a permanent-magnet synchronous motor with high current density," *IEEE Trans. Ind. Electron.*, Vol. 64, No. 3, 2168–2177, Mar. 2017.
5. Yan, L., Z. Dong, and S. Zhang, "Thermal analysis of a novel linear oscillating machine based on direct oil-cooling windings," *IEEE Trans. Energy Convers.*, Vol. 37, No. 2, 1042–1051, Jun. 2022.
6. Xu, Y., B. Zhang, and G. Feng, "Research on thermal capacity of a high-torque-density direct drive permanent magnet synchronous machine based on a temperature cycling module," *IEEE Access*, Vol. 8, 155721–155731, 2020.
7. Song, Z., R. Huang, W. Wang, S. Liu, and C. Liu, "An improved dual iterative transient thermal network model for PMSM with natural air cooling," *IEEE Trans. Energy Convers.*, Vol. 37, No. 4, 2588–2600, Dec. 2022.
8. Gan, C., Y. Chen, X. Cui, J. Sun, R. Qu, and J. Si, "Comprehensive investigation of loss calculation and sequential iterative fluid-solid coupling schemes for high-speed switched reluctance motors," *IEEE Trans. Energy Convers.*, Vol. 36, No. 2, 671–681, Jun. 2021.
9. Yang, C., Y. Zhang, and H. Qiu, "Influence of output voltage harmonic of inverter on loss and temperature field of permanent magnet synchronous motor," *IEEE Trans. Magn.*, Vol. 55, No. 6, 1–5, Jun. 2019.
10. Guo, C., S. Huang, J. Wang, and Y. Feng, "Research of cryogenic permanent magnet synchronous motor for submerged liquefied natural gas pump," *IEEE Trans. Energy Convers.*, Vol. 33, No. 4, 2030–2039, Dec. 2018.
11. Wang, H., J. Chen, Y. Jiang, and D. Wang, "Coupled electromagnetic and thermal analysis of permanent magnet rectifier generator based on LPTN," *IEEE Trans. Magn.*, Vol. 58, No. 2, 1–5, Feb. 2022.
12. Tong, W., R. Sun, S. Li, and R. Tang, "Loss and thermal analysis for high-speed amorphous metal PMSMs using 3-D electromagnetic-thermal Bi-directional coupling," *IEEE Trans. Energy Convers.*, Vol. 36, No. 4, 2839–2849, Dec. 2021.
13. Huang, X., L. Li, B. Zhou, C. Zhang, and Z. Zhang, "Temperature calculation for tubular linear motor by the combination of thermal circuit and temperature field method considering the linear motion of air gap," *IEEE Trans. Ind. Electron.*, Vol. 61, No. 8, 3923–3931, Aug. 2014.
14. Tang, Y., L. Chen, F. Chai, and T. Chen, "Thermal modeling and analysis of active and end windings of enclosed permanent-magnet synchronous In-wheel motor based on multi-block method," *IEEE Trans. Energy Convers.*, Vol. 35, No. 1, 85–94, Mar. 2020.
15. Uzhegov, N., J. Barta, J. Kurfürst, C. Ondrusek, and J. Pyrhönen, "Comparison of high-speed electrical motors for a turbo circulator application," *IEEE Trans. Ind. Appl.*, Vol. 53, No. 5, 4308–4317, Sept.–Oct. 2017.
16. Liu, G., M. Liu, Y. Zhang, H. Wang, and C. Gerada, "High-speed permanent magnet synchronous motor iron loss calculation method considering multiphysics factors," *IEEE Trans. Ind. Electron.*, Vol. 67, No. 7, 5360–5368, Jul. 2020.
17. Li, W., P. Wang, D. Li, X. Zhang, J. Cao, and J. Li, "Multiphysical field collaborative optimization of premium induction motor based on GA," *IEEE Trans. Ind. Electron.*, Vol. 65, No. 2, 1704–1710, Feb. 2018.
18. Zhang, M., W. Li, and H. Tang, "Demagnetization Fault Diagnosis of the Permanent Magnet Motor for Electric Vehicles Based on Temperature Characteristic Quantity," *IEEE Trans. Transp. Electrif.*, Vol. 9, No. 1, 759–770, Mar. 2023.
19. Almandoz, G., I. Gómez, G. Ugalde, J. Poza, and A. J. Escalada, "Study of Demagnetization Risk in PM Machines," *IEEE Trans. Ind. Appl.*, Vol. 55, No. 4, 3490–3500, Jul.–Aug. 2019.